Supplemental Information for

Anti-Bonding Mediated Record Low and Comparable-to-Air Lattice Thermal Conductivity of Two Metallic Crystals

Zhonghua Yang[1,#], Wenbo Ning[1,#], Alejandro Rodriguez[2], Lihua Lu[1], Junxiang Wang[1], Yagang Yao[4], Kunpeng Yuan[3,*], and Ming Hu[2,*]

[1]College of Architecture and Civil Engineering, Shenyang University of Technology, Shenyang, 110870, China

[2]Department of Mechanical Engineering, University of South Carolina, Columbia, 29201, USA

[3]College of New Energy, China University of Petroleum (East China), Qingdao 266580, China

[4]National Laboratory of Solid State Microstructures, College of Engineering and Applied Sciences, Jiangsu Key Laboratory of Artificial Functional Materials, and Collaborative Innovation Center of Advanced Microstructures, Nanjing University, Nanjing 210093, China

[#]These authors contributed equally to this work.

[*]Author to whom all correspondence should be addressed. E-Mails: yuankunpengupc@163.com (K.Y.), hu@sc.edu (M.H.)

In this work, all the self-consistent Density Functional Theory (DFT) and Density Functional Perturbation Theory (DFPT) calculations are implemented in Quantum Espresso (QE)[1]. The convergence of total energy with respect to *K*-points density, energy cut-off, and smearing energy have been carefully checked. The input atomic structure is optimized to ensure the stability of lattice structure. In all the structure optimization DFT calculations, *K*-points of 21 × 21 × 21 and 13 × 13 × 13 gamma grid are set for pure metals and intermetallic compounds, respectively. A plane-wave energy cutoff of 70 Ry for the truncation of the plane wave basis is set for all the calculations. In these calculations, the Ultra Soft Pseudo Potentials (USPP) and Generalized Gradient Approximation (GGA) functional are used in our calculations. The lattice structure and the optimized lattice constant are listed in **Table S1**, in which the DFT calculated lattice constants are compared with the experimental values[2, 3].

Table S1. Lattice structure and lattice constant of metals in our work and experimental lattice constants are also presented for comparisons. 2nd IFCs and 3rd IFCs are obtained through CSLD. NN represents the nearest neighbors.

Materials	Lattice constant		Input in CSLD[4]			
	DFT (Å)	Exp. (Å)	Supercell	NN	Cutoff (Å)	*K*-points
Pd	3.917	3.950[2]	5×5×5	5	6.527	4×4×4
Ag	4.129	4.078[5]	4×4×4	5	6.897	4×4×4
PbAuGa	6.702		3×3×3	3	5.156	2×2×2
CsKNa	9.985		3×3×3	3	7.673	2×2×2

In *p-p* scattering rate calculations, to obtain Interatomic Force Constants (2nd IFCs and 3rd IFCs) efficiently, CSLD method is used. The inputs in CSLD have been listed in **Table S1**. Considering the computational cost and precious, the nearest neighbors (NN) have been set to 5 for pure metal and 3 for intermetallic compounds. Furthermore, in order to quantify the strength of interatomic interactions which are described by harmonic IFCs, we calculated the normalized

trace of interatomic force constant tensors[6]. According to this parameter, one can directly determine how large the cutoff radius should be used to evaluate the anharmonic IFCs by effectively including the possibly strong interaction strength as revealed by the large trace value. **Figure S1(a)** is the normalized trace of IFC in Pd, it is clear that when the cutoff radius is less than 6.527 Å (red ball), which are corresponding to the 5th-nearest neighbors of Pd, there exist strong interactions. When the cutoff radius is bigger than the threshold value (5th-nearest neighbor), the trace values turn out to be very weak, indicating negligible force constants. Similarly, the cutoff has been set as 6.897 Å, 5.1516Å, and 7.673Å for Ag, PbAuGa, and CsKNa respectively.

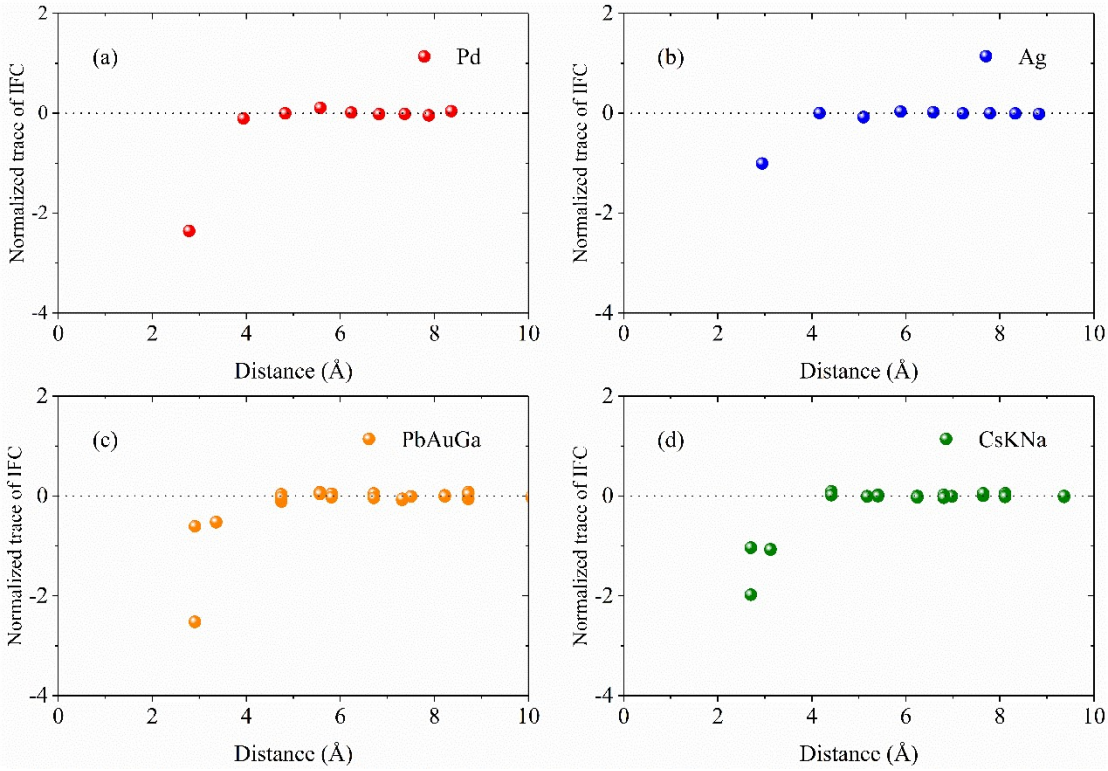

Figure S1. Normalized trace of interatomic force constant tensors *vs* atomic distances.

In *p-e* scattering rate calculations, the phonon perturbation is firstly calculated using DFPT as implemented in QE and then the *p-e* scattering matrix element is calculated in Electron-Phonon Wannier (EPW) package[7]. The *p-e* scattering matrix element is initially obtained on coarse electron and phonon wave vector grids and then interpolated to denser electron and phonon wave vector grids using the maximally localized Wannier function basis as implemented in EPW. The

Q- and *K*-points of Coarse meshes and Finer meshes are listed in **Table S2**. Finally, the *p-e* scattering rate contributed to phonon and electron transport can be obtained. To make sure the accuracy of EPW, we can now compare the interpolated band structures (EPW) with those from the *ph.x* module in QE [see **Figure S2**]. It indicates the reliability of the calculated.

Table S2. Number of Maximally Localized Wannier Functions (MLWFs) for the *p-e* matrix interpolation. Coarse and finer mesh of phonon and electron wave vector for calculating the *p-e* scattering rate in EPW.

Materials	Coarse meshes		Finer meshes	
	Q-points	*K*-points	*Q*-points	*K*-points
Pd	3×3×3	6×6×6	15×15×15	30×30×30
Ag	3×3×3	9×9×9	18×18×18	30×30×30
PbAuGa	4×4×4	12×12×12	15×15×15	30×30×30
CsKNa	2×2×2	12×12×12	20×20×20	30×30×30

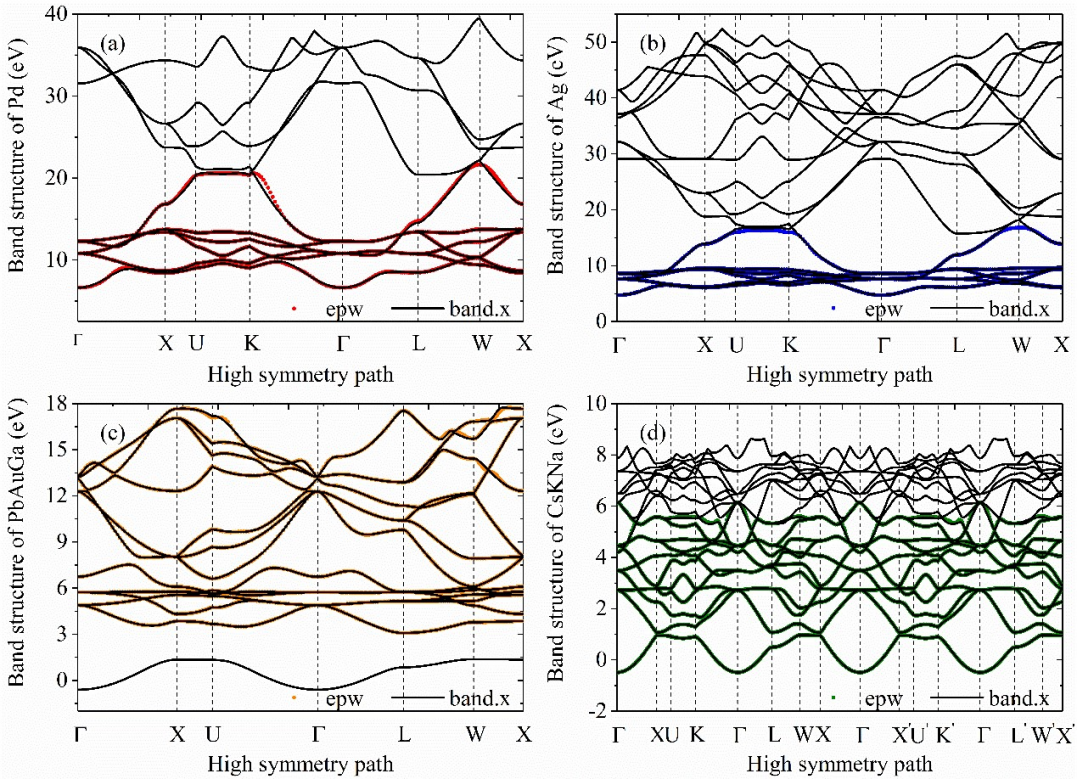

Figure S2. The comparison of the interpolated band structures (EPW) with those from the *ph.x* module in

QE.

In thermal conductivity calculations, the ShengBTE package[8] was modified to incorporate the *p-e* scattering and *p-p* scattering. The thermal conductivity convergence of PbAuGa and CsKNa with respect to the *Q*-grids is fully examined in **Figure S3**. It is shown in **Figure S3** that the thermal conductivity of PbAuGa possesses a well-converged behavior when the *Q*-grids are greater than 15 × 15 × 15, and for CsKNa, the *Q*-grids will be set as 20 × 20 × 20.

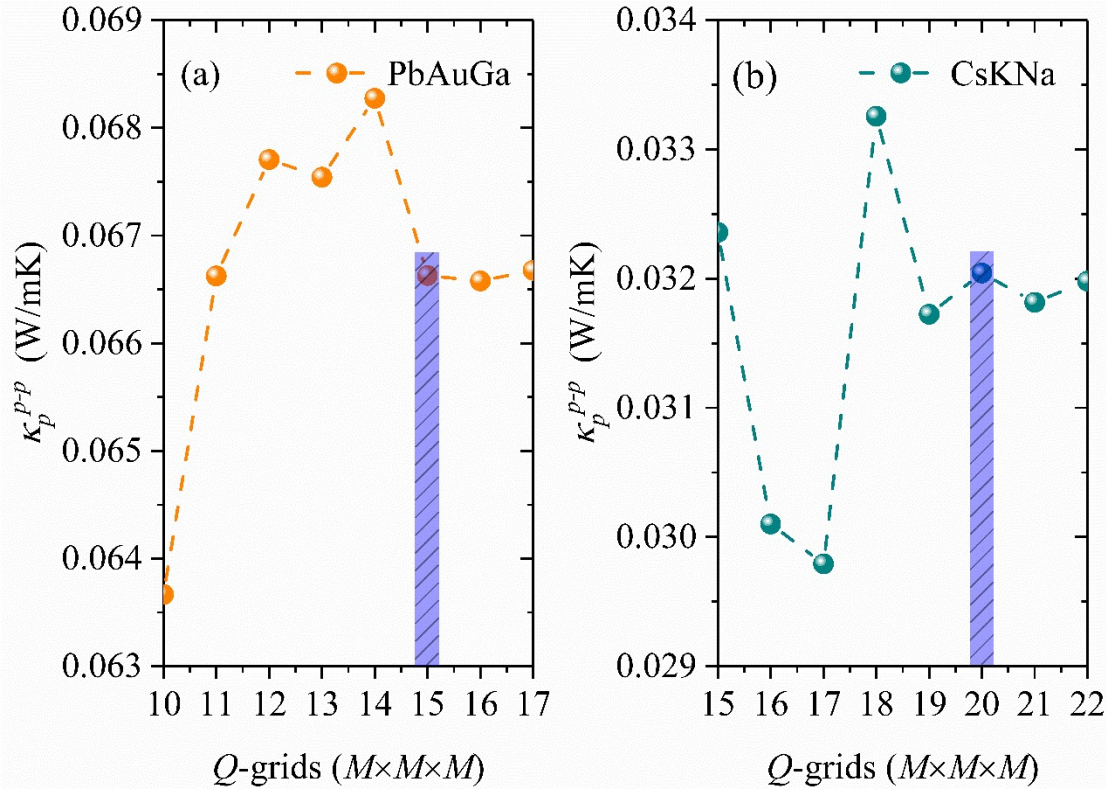

Figure S3. The thermal conductivity convergence of PbAuGa and CsKNa with respect to the *Q*-grids.

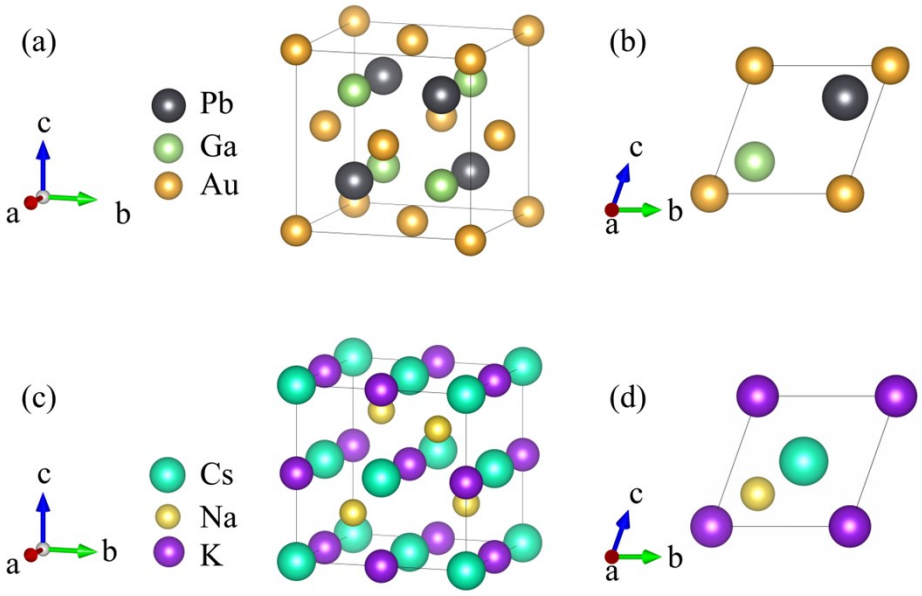

Figure S4. Crystal structure of PbAuGa and CsKNa. (a) and (c) are the perspective views of unit cells for PbAuGa and CsKNa, respectively. (b) and (d) are the side views of corresponding primitive cells.

Elastic constants are physical properties of crystals to relate the mechanical response to the material deformation. The elasticity tensor is a fourth-rank tensor describing the stress-strain relation in a linear elastic material, but the elasticity tensor only has at most 21 independent components due to symmetry. For cubic crystals the elastic constant, C_{ij}, may be reduced to just three independent elastic constants: C_{11}, $C_{12,}$ and C_{44}. The elastic constants of Pd, Ag, PbAuGa, and CsKNa are listed in **Table S3**. Coudert[9] states the generic requirements for the elastic stability of crystal lattices and gives simplified equivalents of the generic conditions for some high-symmetry crystal classes. In particular, in the case of cubic crystals, the conditions of stability reduce to a very simple form:

$$C_{11} - C_{12} > 0, C_{11} + 2C_{12} > 0, C_{44} > 0 \quad (1)$$

Therefore, from the table, it is clear that the elastic constants of PbAuGa and CsKNa satisfy the stability criteria, and the compounds are mechanically stable.

Table S3. Calculated elastic constants (C_{ij}) (in GPa), Young's modulus (in GPa) (E), Shear modulus (in GPa) (G)

	C_{11} (GPa)	C_{12} (GPa)	C_{44} (GPa)	E (GPa)	G (GPa)	Mechanical stability criteria[9]
Pd	205.90	150.72	61.84	131.91	48.14	Criteria (i) C_{11} - C_{12} > 0 met. Criteria (ii) C_{11} + 2C_{12} > 0 met. Criteria (iii) C_{44} > 0 met.
Ag	101.47	81.10	29.98	61.08	22.06	
PbAuGa	71.09	45.50	3.97	21.50	7.50	
CsKNa	4.77	1.82	0.03	1.70	0.61	

It is important to verify the energy stability of PbAuGa and CsKNa, which is helpful for judging whether they can be synthesized experimentally. The cohesive energy of a solid refers to the energy required to separate constituent atoms apart from each other and to bring them to an assembly of neutral free atoms[10], it is a widely accepted parameter used to evaluate the stability of materials. We calculate the cohesive energy E_{coh} using the following formulas[11]:

$$E_{coh} = \frac{E_A + E_B + E_c - E_{ABC}}{3} \qquad \text{* MERGEFORMAT (2)}$$

where E_A, E_B, and E_C are the total energy of three isolated elements in PbAuGa, respectively, E_{ABC} is the total energy of the PbAuGa. If E_{ABC} is lower than the sum of E_A, E_B, *and* E_C, E_{coh} will be positive meaning the PbAuGa and CsKNa could exist in a stable crystalline state rather than in a free (single element) state.

Table S4. The energy of compounds and isolated elements in PbAuGa and CsKNa

	Energy (Ry)		Energy (Ry)
PbAuGa	-391.88	CsKNa	-209.86
Pb	-135.21	Cs	-54.05
Au	-85.17	K	-58.72
Ga	-170.85	Na	-96.93

According to the data shown in **Table S4**, the calculated cohesive energies are 0.22 Ry/atom,

and 0.053 Ry/atom for CsKNa and PbAuGa, respectively. The positive cohesive energies demonstrate the stability of PbAuGa and CsKNa, which is a necessary condition for experimental synthesis.

The cumulative κ_p^{p-p} as a function of frequency for Pd, Ag, PbAuGa, and CsKNa are displaced in **Figure S5**, it is clear that the cumulative κ_p^{p-p} of all four systems increase with the frequency, but the cumulative κ_p^{p-p} of PbAuGa and CsKNa increase faster than that of Pd and Ag in low frequency range. It means the acoustic modes of PbAuGa and CsKNa contribute the most to κ_p^{p-p}, being about 76% and 78%, respectively. Compared with the other three systems, there is a peak appeared in the cumulative κ_p^{p-p} curve of CsKNa after the frequency of 2 THz which is the HLO frequency range. The contribution of HLO in CsKNa (12%), which is higher than the counterpart of PdAuGa (5%), the κ_p^{p-p} peak can also be found in **Figure 2(b)**.

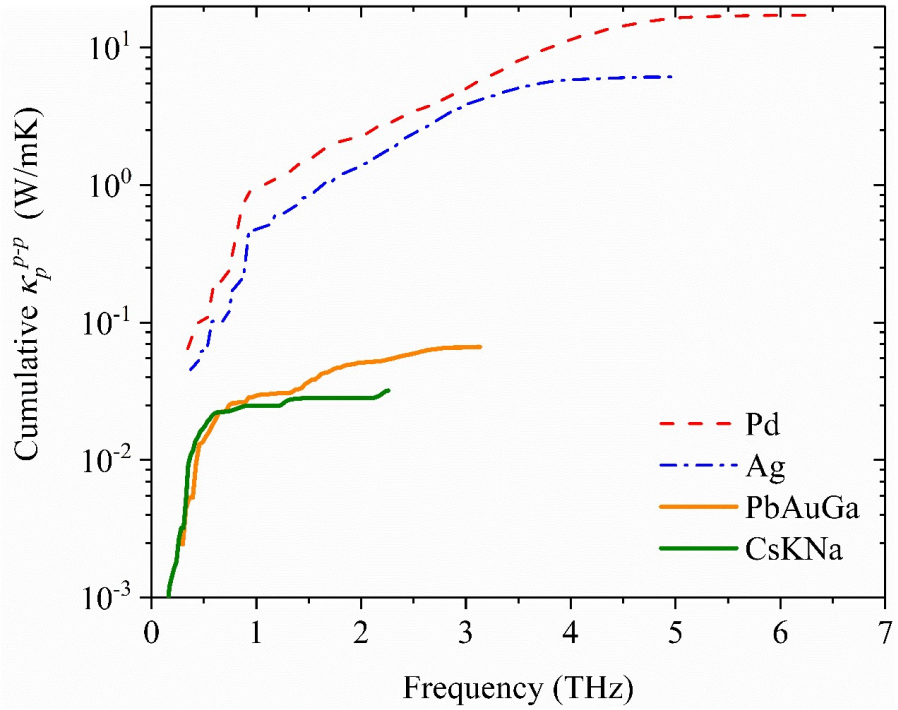

Figure S5. The cumulative κ_p^{p-p} as a function of frequency for Pd, Ag, PbAuGa, and CsKNa.

Figure S6 shows the potential energy change with respect to the displacement of Au and Cs atoms along the eigenvector of the LA branch. The displacement factor=0 on the *x-axis* means that the atom is in the equilibrium position, and the absolute value of the displacement factor increasing means that the amplitude of the atom vibrates around the equilibrium position. The dashed blue and black lines represent the perfect harmonic behavior of PbAuGa and CsKNa, respectively. It is found that the potential wall becomes nonlinear with the displacement factor increasing, indicating more asymmetry dependence of restoring forces on atomic displacement amplitudes[12, 13]. Compared to the potential wall of PbAuGa, the potential wall of CsKNa deviates from the harmonic behavior more pronounced, implying stronger phonon anharmonic behavior. We conclude that rattlers Au and Cs in PbAuGa and CsKNa respectively, act as loosely bonded atoms, reduce phonon harmonic behavior, and thus lower the κ_p^{p-p} of PbAuGa and CsKNa, respectively.

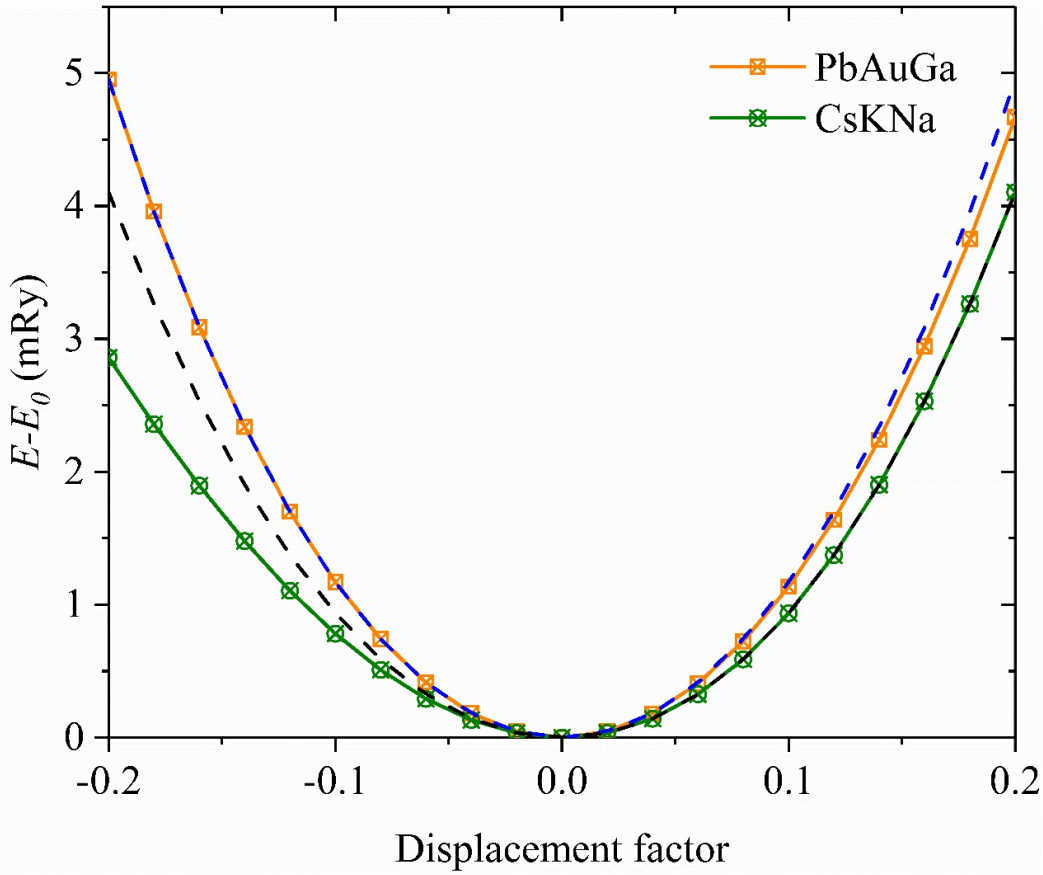

Figure S6. The potential energy of PbAuGa and CsKNa as a function of displacement factor. The dashed lines are fitting curves by perfect harmonic formula.

To understand the chemical bonding environment in PbAuGa and CsKNa, we further calculated the electron localization function (ELF) since ELF is a simple measure of electron localization in an atomic and molecular system. The ELF values are defined between 0 and 1, in which ELF = 1 means the perfect localization and ELF = 0.5 corresponds to the electron gas. Here the ELFs of nearest neighbor composite elements in PbAuGa and CsKNa are shown in **Figure S7**, including the perspective view of ELFs in **Figure S7 (a) and (c)**, and the plane view of ELFs in **Figure S7 (b) and (d)**. The following can be learned: Au and Cs atoms act as the rattlers, and their physical binding feature accounts for the global weak bonding environment in PbAuGa and CsKNa. It should be noted that electron cloud is mainly occupied between Au-Pb and Au-Ga atoms, and the weak interaction is the key determinant in the structural unit. It is more obvious in the CsKNa that the Na atom possesses an asymmetrically distributed electron cloud, with a higher localized electron between the K-Na bond illustrating the covalent bonding. In contrast, the atomic density of Na atoms in the opposite direction is very weak, which is due to rattle atom Cs. A similar conclusion can also be found in paper[14], where Bi_5CuS_8 exhibits a low κ_l, of around 0.6 W/mK, and the corresponding microscopic mechanism originates from the anharmonic and anisotropic vibration of the Cu atom, the ionic bond feature around the Cu atom, and the global weak bonding.

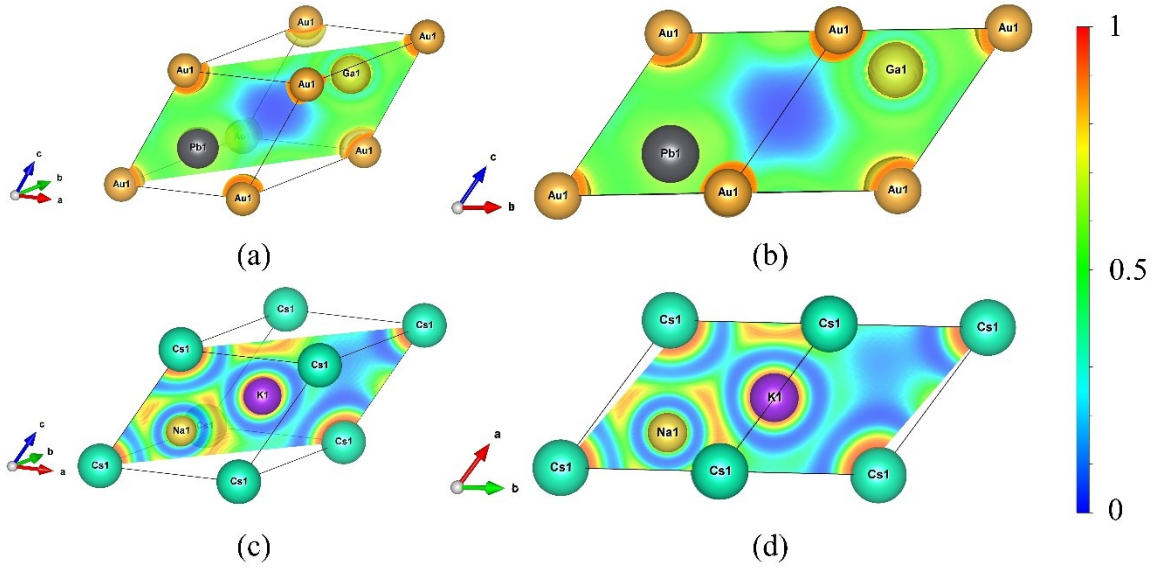

Figure S7. The ELFs of PbAuGa and CsKNa. (a) and (c) the perspective view of ELF, (c) and (d) the plane view of ELF

The contribution of phonon thermal conductivity on thermal conductivity is quantified by $\kappa_p^{p-e} \Big/ \kappa_{total}^{DFT}$, the raw data κ_p^{p-p}, κ_p^{p-e}, and κ_e^{p-e} of 21 pure metals and intermetallic compounds is listed in **Table S5**. Some of the data is from reference[15]. In **Table S5**, the DFT predictions of electrical conductivity σ and total thermal conductivity $\kappa_{total}^{DFT} = \kappa_p^{p-e} + \kappa_e^{p-e}$. κ_p^{p-e} denotes the phononic thermal conductivity considering *p-e* coupling, κ_e^{p-e} denotes the electronic thermal conductivity considering *p-e* coupling. Furthermore, the effect of *p-e* coupling on phonon thermal conductivity is determined by $\left(\kappa_p^{p-p} - \kappa_p^{p-e}\right) \Big/ \kappa_p^{p-p}$. We relate the increase in thermal conductivity to the estimated electronic component of the thermal conductivity using the Wiedemann-Franz law, and find that our data are consistent with conventional Sommerfeld value of the Lorenz number.

Table S5. The raw data κ_p^{p-p}, κ_p^{p-e}, and κ_e^{p-e} of 21 pure metals and intermetallic compounds. $L_0 = \pi^2 k_B^2 / (3e^2) = 2.44 \times 10^{-8} V^2 K^{-2}$ is the Sommerfeld value of the Lorenz number[16], $L = \kappa_e^{p-e} / (\sigma T)$, where T is the temperature. The data other than Pd, Ag, PbAuGa, and CsKNa are taken from Ref.[15].

System	κ_p^{p-p} (W/mK)	κ_p^{p-e} (W/mK)	κ_e^{p-e} (W/mK)	κ_{total}^{DFT} (W/mK)	$\kappa_p^{p-e} / \kappa_{total}^{DFT}$ (%)	$(\kappa_p^{p-p} - \kappa_p^{p-e}) / \kappa_p^{p-p}$ (%)	σ ($\times 10^7\ \Omega^{-1}\ m^{-1}$)	$\frac{L}{L_0}$
Pd	20.15	14.25	80.45	94.7	15.05	29.28	1.39	0.79
Ag	6.11	5.86	396.49	402.35	1.46	4.09	5.5	0.98
Pb	1.12	0.89	43.31	44.2	2.01	20.54	0.59	1.00
Au	3.05	2.80	273.45	276.25	1.01	8.20	3.63	1.03
Cu	19.49	17.42	361.32	378.74	4.60	10.62	5.27	0.94
Al	10.02	8.95	232.53	241.49	3.71	10.68	3.37	0.94
Mg	9.27	7.15	178.20	185.35	3.86	22.87	2.43	1.00
Pt	8.67	6.49	89.75	96.24	6.74	25.14	1.23	1.00
Ni	27.79	15.33	84.53	99.86	15.35	44.84	1.51	0.76
Ti	11.92	5.32	25.31	30.63	17.37	58.3	0.38	0.91
Co	20.60	12.99	78.65	91.65	14.17	36.94	1.16	0.92
Mn	6.17	3.02	4.98	8.00	37.75	51.05	0.08	0.86
NiAl	12.31	6.02	63.89	69.91	8.61	51.10	0.86	1.02
Ni_3Al	7.78	4.72	31.95	36.66	12.88	39.33	0.43	1.02
TiAl	7.88	5.17	7.34	12.51	41.33	34.39	0.10	0.96
FeAl	7.25	3.24	8.49	11.72	27.65	55.31	0.13	0.90
CoAl	9.81	4.83	40.85	45.67	10.58	50.76	0.59	0.95
Cu_3Au	2.37	1.89	118.36	120.25	1.57	20.25	1.66	0.98
CuAu	3.32	2.32	132.46	134.78	1.72	30.12	1.83	0.99
PbAuGa	0.066	0.064	17.42	17.48	0.37	3.03	0.24	0.99
CsKNa	0.032	0.031	10.76	10.80	0.29	3.13	0.16	0.92

In order to consider the effect of *p-e* coupling on phononic thermal conductivity, we compare the scattering rate with or without *p-e* coupling in **Figure S8**. Combining **Figure 7** and **Table S5**, Pd and CsKNa are chosen as representatives due to their $\left(\kappa_p^{p-p}-\kappa_p^{p-e}\right)/\kappa_p^{p-p}$ exist big differences. It is obvious that scattering rates of Pd, PbAuGa, and CsKNa are enhanced when the *p-e* coupling is considered, leading to lower phononic thermal conductivity. Comparatively speaking, the change of PbAuGa and CsKNa scattering rate is very tiny, indicating the weak *p-e* coupling effect which is consistent with the value $\left(\kappa_p^{p-p}-\kappa_p^{p-e}\right)/\kappa_p^{p-p}$ in **Figure 7**.

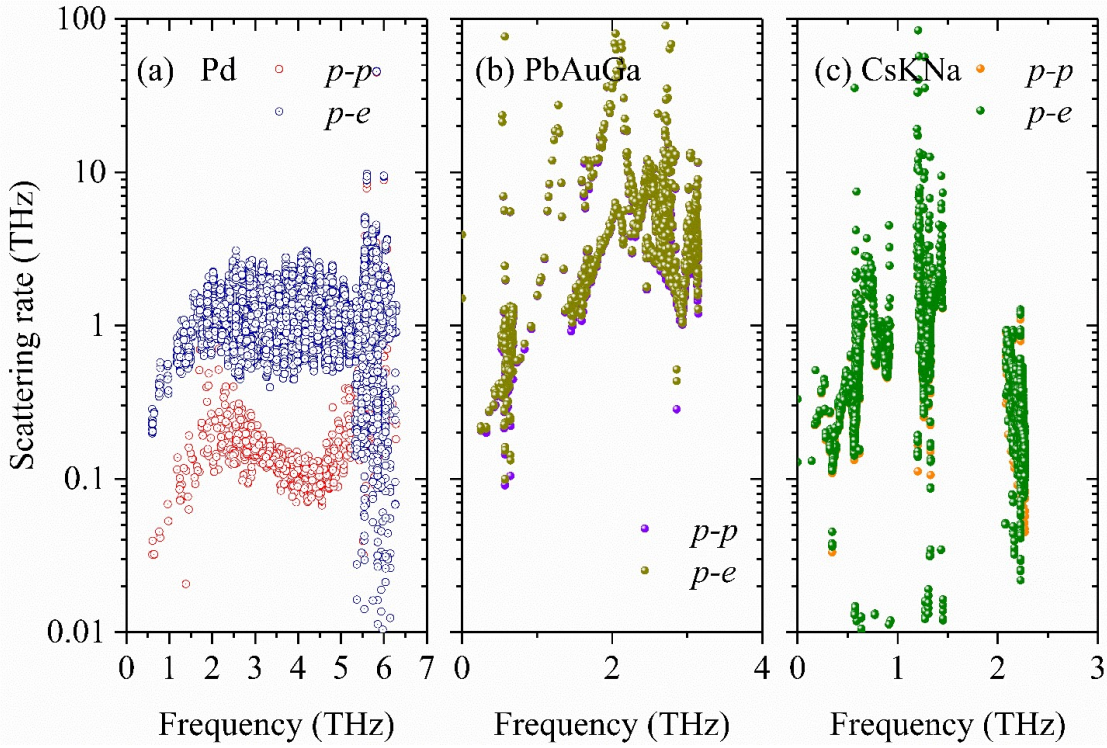

Figure S8. Comparison of *p-e* and *p-p* coupling scattering rate of (a) Pd, (b) PbAuGa, and (c) CsKNa.

Reference

[1] GIANNOZZI P, BARONI S, BONINI N, CALANDRA M, CAR R, CAVAZZONI C, CERESOLI D, CHIAROTTI G L, COCOCCIONI M, DABO I, DAL CORSO A, DE GIRONCOLI S, FABRIS S, FRATESI G, GEBAUER R, GERSTMANN U, GOUGOUSSIS C, KOKALJ A, LAZZERI M, MARTIN-SAMOS L, MARZARI N, MAURI F, MAZZARELLO R, PAOLINI S, PASQUARELLO A, PAULATTO L, SBRACCIA C, SCANDOLO S, SCLAUZERO G, SEITSONEN A P, SMOGUNOV A, UMARI P, WENTZCOVITCH R M. QUANTUM ESPRESSO: a modular and open-source software project for quantum simulations of materials [J]. Journal of Physics: Condensed Matter, 2009, 21(39): 395502.

[2] HULL A W. X-Ray Crystal Analysis of Thirteen Common Metals [J]. Physical Review, 1921, 17(5): 571-588.

[3] JETTE E R, FOOTE F. Precision Determination of Lattice Constants [J]. The Journal of Chemical Physics, 1935, 3(10): 605-616.

[4] ZHOU F, NIELSON W, XIA Y, OZOLIŅŠ V. Lattice Anharmonicity and Thermal Conductivity from Compressive Sensing of First-Principles Calculations [J]. Physical Review Letters, 2014, 113(18): 185501.

[5] JETTE E R, FOOTE F. Precision Determination of Lattice Constants [J]. The Journal of Chemical Physics, 2004, 3(10): 605-616.

[6] LEE S, ESFARJANI K, LUO T, ZHOU J, TIAN Z, CHEN G. Resonant bonding leads to low lattice thermal conductivity [J]. Nature Communications, 2014, 5(1): 3525.

[7] PONCé S, MARGINE E R, VERDI C, GIUSTINO F. EPW: Electron-phonon coupling, transport and superconducting properties using maximally localized Wannier functions [J]. Computer Physics Communications, 2016: 116-133.

[8] LI W, CARRETE J, KATCHO N, MINGO N. ShengBTE: A solver of the Boltzmann transport equation for phonons [J]. Computer Physics Communications, 2014, 185: 1747–1758.

[9] MOUHAT F, COUDERT F-X. Necessary and sufficient elastic stability conditions in various crystal systems [J]. Physical Review B, 2014, 90(22): 224104.

[10] MIZUTANI U, INUKAI M, SATO H, ZIJLSTRA E S. 2 - Electron Theory of Complex Metallic Alloys [M]//LAUGHLIN D E, HONO K. Physical Metallurgy (Fifth Edition). Oxford; Elsevier. 2014: 103-202.

[11] BO T, LIU P-F, YAN L, WANG B-T. Electron-phonon coupling superconductivity in two-dimensional orthorhombic MB$_6$ (M=Mg, Ca, Ti, Y) and hexagonal MB$_6$ (M=Mg, Ca, Sc, Ti) [J]. Physical Review Materials, 2020, 4(11): 114802.

[12] ZHAO L-D, CHANG C, TAN G, KANATZIDIS M G. SnSe: a remarkable new thermoelectric material [J]. Energy & Environmental Science, 2016, 9(10): 3044-3060.

[13] ZEIER W G, ZEVALKINK A, GIBBS Z M, HAUTIER G, KANATZIDIS M G, SNYDER G J. Thinking Like a Chemist: Intuition in Thermoelectric Materials [J]. Angew Chem Int Ed, 2016, 55: 6826-6841.

[14] LIU Z, ZHANG W, GAO W, MORI T. A material catalogue with glass-like thermal conductivity mediated by crystallographic occupancy for thermoelectric application [J]. Energy & Environmental Science, 2021, 14(6): 3579-3587.

[15] TONG Z, LI S, RUAN X, BAO H. Comprehensive first-principles analysis of phonon thermal conductivity and electron-phonon coupling in different metals [J]. Physical Review B, 2019, 100(14): 144306.

[16] KLEMENS P G, WILLIAMS R K. Thermal conductivity of metals and alloys [J]. International Metals Reviews, 1986, 31(1): 197-215.